

Simulation of birefringence effects for high-energy neutrino detectors

This report has been carried out by Nils Heyer at the
Department of Physics and Astronomy of Uppsala University
under the supervision of
Dr. Christian Glaser

Abstract

The detection of high-energy neutrinos in the $E > \mathcal{O}(\text{PeV})$ range requires new detection techniques in order to cope with the decreasing flux. The radio detection method uses Askaryan emission to detect these neutrinos. The propagation of the radio pulses has to be modeled carefully in order to estimate the properties of the neutrinos from the detected radio pulse. This report introduces a model which was implemented to the NuRadioMC code to simulate birefringence effects in the ice of the South Pole. To do that, a new ice model was created which combines the density and directional dependence on the refractive index. With this ice model and an analytical ray tracer the time delay and polarization resulting from birefringence was simulated for different geometries. A directional dependence on the magnitude of the time delay and the change of the polarization along the propagation path was found. To model the mixing of the polarization states due to this change in polarization a pulse propagation model was introduced. Time delay calculations resulting from this model were compared to simulations and measurements from the ARA experiment and have shown good agreement.

Contents

1	Introduction	1
1.1	Radio Detection of Cosmic Neutrinos	1
1.2	NuRadioMC	2
1.3	Birefringence Effect	3
2	'Regular' Biaxial Birefringence	4
2.1	Effective Refractive Index	4
2.2	Time Delay and Polarization	6
3	Modeling the refractive index of the Antarctic ice	7
3.1	Southpole 2015 Model	7
3.2	SPICE Data	8
3.3	Merging of the two Models	10
4	Pulse Propagation	11
4.1	Analytical Ray Tracer	11
4.2	Pulse Propagation due to Changing Polarization	12
5	Results for different Geometries	16
5.1	Comparing the model to ARA measurements	17
5.2	Numerical accuracy	21
6	Summary and Outlook	23
	References	25

1 Introduction

The neutrino is perhaps the least understood particle of the standard model. Many questions like the absolute mass of the neutrino or the absence of right handed neutrinos in weak interactions remain unanswered. However, neutrinos have certain properties that make them very interesting in terms of probing astrophysical objects. They are stable and only interact via the weak force with a relatively small cross section. In this way they are less likely to be absorbed between a possible source and a detector than for example photons. Secondly, neutrinos don't carry an electric charge so they can't be deflected by electric or magnetic fields on their path. This means that when measuring a neutrino in a detector, the direction it came from points directly back at the source at which it was created. This makes neutrino detection extremely valuable in the field of multi messenger astronomy. Problematically, the properties that make neutrinos the ideal messenger particle also make it difficult to detect them, especially their small cross section and the neutral electric charge. This results in neutrino detectors utilizing bigger and bigger target mediums, usually ice or water. However, the flux of neutrinos hitting the earth is dominated by solar neutrinos in the keV to MeV range. When looking at higher energies the neutrino flux drops drastically and the sources of the highest energy cosmic neutrinos in the above PeV range remain largely unknown [1].

So far, neutrino detection mostly relied on photo multipliers capturing the visible part of the Cherenkov light emitted after a neutrino interaction. Due to the low flux of high-energy neutrinos more target material has to be utilized to detect them. This becomes very expensive when relying on photo multipliers that, in the case of ice as target material, are reliant on kilometer deep boreholes. New methods based on radio antennas strive to extend the energy range of neutrino telescopes [2, 3, 4]. The development of those detectors needs precise models of the medium and the radio signal propagation. This report focuses on the effect birefringence has on the radio signal propagation in the ice of the South Pole.

1.1 Radio Detection of Cosmic Neutrinos

When a high-energy neutrino interacts in a target material via neutral or charged current interactions, the nucleus of the target atom is destroyed and many secondary particles are generated in a particle shower. All shower particles, satisfying the relation $\beta n > 1$, emit Cherenkov radiation while the shower size scales with the neutrino energy. The shower grows exponentially until the initial energy is deposited in the medium. Since the positrons created in the shower annihilate in the target medium and the shower electrons drag other electrons from the medium along, the shower front is dominated by electrons. This time varying charge imbalance results in a dipole that emits electromagnetic waves in the radio frequency range (MHz - GHz). This phenomenon is known as the Askaryan effect. As the radio waves traverse through the target medium towards the antenna many effects like refraction, reflection, attenuation

or polarization have to be taken into account. Especially interesting is the change of density depending on the depth. This results in a change of the refractive index, especially in the top ~ 300 m of the ice also known as firn. This change results in the radio signals bending downwards as seen in figure 1. Due to this bending, signals from certain positions can't reach the antenna at all (shadow zone). However, the bending also leads to many radio waves that would otherwise have missed the detection antenna getting refracted downwards. The antennas are usually deployed in surface stations that use LPDA (log-periodic dipole antennas) pointing in different directions including upwards to discriminate against air showers. Many ideas for the design of these stations also include a slot antenna at about 150 m depth. In this way the detection of rays that were refracted downwards in the firn of the ice is enabled. This report exclusively focuses on antennas deployed at 150 m depth but the principle of birefringence induced time delay could also be used for more shallow stations.

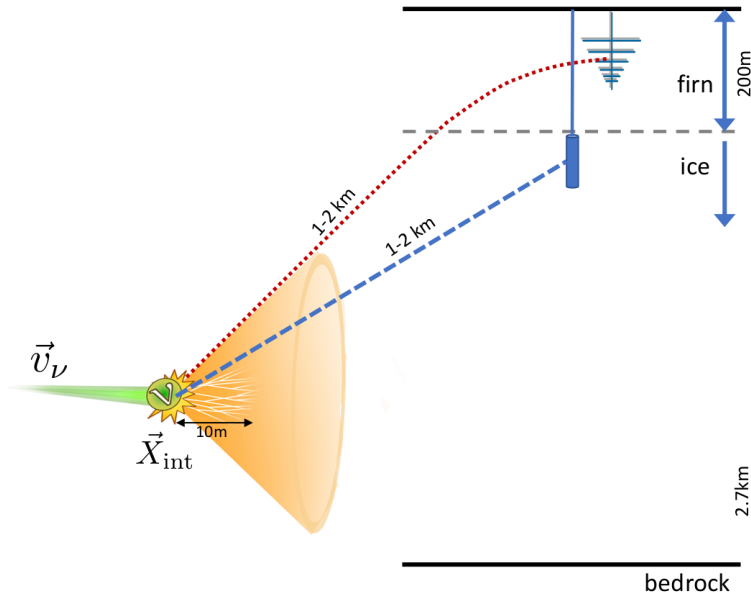


Figure 1: Sketch of Askaryan radiation in ice. Figure taken from [5]. The incoming neutrino interacts in the ice and sends out a particle shower. The shower induces radio waves that propagate through the ice and get detected by LPDA and slot antennas.

1.2 NuRadioMC

NuRadioMC [6] is a framework designed to simulate neutrino interactions and their detection via radio waves. All steps, including the initial interaction, the radio emission due to the Askaryan effect, the signal propagation and the measured signal by the antennas, can be simulated using NuRadioMC. The Monte Carlo simulations made possible by NuRadioMC offer the opportunity to set requirements for the experiment and optimize the radio detectors. For the hardware side this has an impact on the

detector/station layout, the calibration specifications and the trigger level. From the software side NuRadioMC can be used to create training sets to be able to reconstruct the neutrino properties from the signal shape using deep learning. In a simulation using NuRadioMC first an event list is generated with the energies, directions, and interaction points of the specified number of neutrinos as a .hdf5 file. The next step takes the event list and simulates the Askaryan signal generation, the signal propagation and the detector output. The obtained simulation data can be visualized using histograms. The following model was implemented into the signal propagation script of NuRadioMC but not yet used by a full simulation. This report only focuses on describing the included model and how it compares to other birefringence models and measurements.

1.3 Birefringence Effect

The optical properties of transparent crystals can be categorized by how the relative permittivity behaves along different directions. Isotropic crystals have a cubic structure which results in the same optical properties in all directions. As such they have the relative permittivities of $\epsilon_x = \epsilon_y = \epsilon_z$. This includes materials like glass or sodium chloride. Uniaxial crystals have a trigonal, tetragonal or hexagonal structure which results in the same optical properties in two directions and different properties for the third direction. As such they have the relative permittivities of $\epsilon_x = \epsilon_y \neq \epsilon_z$. This includes materials like rubies or quartz. Biaxial crystals have a orthorhombic, monoclinic or triclinic structure which results in different optical properties in all directions. As such they have the relative permittivities of $\epsilon_x \neq \epsilon_y \neq \epsilon_z$. For an incident electromagnetic wave entering a material, both the uniaxial medium and the biaxial medium split the wave as parts of the wave get refracted stronger than others depending on their polarization. This effect is called birefringence [7].

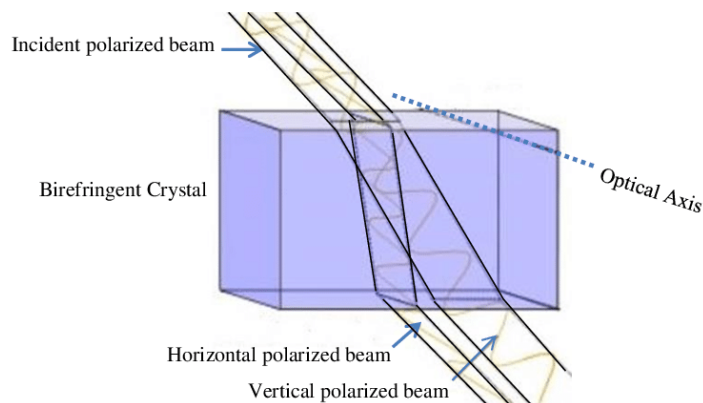


Figure 2: Birefringence in a crystal due to different refraction for different polarizations. Figure taken from [8].

In a uniaxial medium birefringence happens only for one directional axis, for a

biaxial medium it happens for every incoming direction. Due to their different paths and polarization the two waves 'see' different indices of refraction which determines the phase velocity at which the wave propagates. As such there is a time delay between different polarization states with which they reach a potential antenna depending on the directional indices-of-refraction, the propagation direction and the propagation length. With its hexagonal structure ice crystals could be considered uniaxial. However, due to mechanical stress in large amounts of ice such as in Antarctica the ice layers shift into a collective direction. This process is called ice flow and it causes the antarctic ice to become biaxial birefringent.

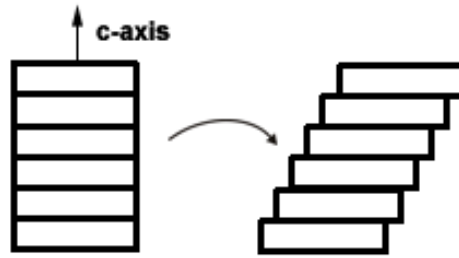


Figure 3: The hexagonal structure planes of the crystal are perpendicular to the c-axis. The crystals deform by gliding along the basal planes. [9]

2 'Regular' Biaxial Birefringence

A 'regular' birefringent medium has different indices of refraction in different directions. However, those stay constant along the propagation path of the wave. This is not the case for the ice of the South Pole since there is a big density dependency involved. Yet, the principle calculations for the birefringence effect are the same. This chapter will focus on those calculations and the resulting time delay and polarization of the wave. Chapter 3 will then illustrate how this effect was combined with the density dependency of the South Pole.

2.1 Effective Refractive Index

When electromagnetic waves travel through a biaxial medium the wave splits into two distinctly polarized waves that take slightly different paths. The velocities of the two polarization states (ordinary- and extraordinary ray) are different as well, which results in a small time delay when the signals are measured by antennas. Modeling this time delay and the polarization of the radio waves at the South Pole was the main objective of this report in order to model the signal propagation more accurately. In theory, this effect can also be used to estimate the distance from the antenna to the interaction point of the initial neutrino.

Using Maxwell's equations one can derive the solutions for harmonic plane waves. From there, the wave equation can be used to calculate the effective refractive index in a birefringent material:

$$\begin{aligned}\vec{\nabla} \times \vec{E} &= -\frac{\partial \vec{B}}{\partial t} \\ \vec{\nabla} \times \vec{B} &= \mu_0 \vec{j} + \mu_0 \epsilon_0 \frac{\partial \vec{E}}{\partial t}\end{aligned}\quad (1)$$

Here, μ_0 is the vacuum permeability, ϵ_0 is the vacuum permittivity and \vec{E} and \vec{B} are the electric field and the magnetic flux density. In the absence of currents and with the \vec{E} and \vec{B} fields written as plane waves the following expression can be derived.

$$\begin{aligned}\vec{k} \times \vec{E} &= \omega \mu_0 \vec{H} \\ \vec{k} \times \vec{H} &= -\omega \epsilon \vec{E}\end{aligned}\quad (2)$$

Here, \vec{k} is the wave vector, ω is the frequency, ϵ is the absolute permittivity and \vec{H} is the magnetic field of the plane wave. The wave equations can then be expressed via the propagation direction \vec{s} (normalized), the speed of light c and the relative permittivity of the medium ϵ_r .

$$\vec{s}(\vec{s} \cdot \vec{E}) - \vec{E} + \frac{\omega^2}{k^2 c^2} \epsilon_r \cdot \vec{E} = 0 \quad (3)$$

With the effective refractive index $n = kc/\omega$ this can be written in matrix form by using the biaxial dielectric tensor ϵ_r .

$$\epsilon = \epsilon_0 \epsilon_r = \epsilon_0 \begin{pmatrix} n_x^2 & 0 & 0 \\ 0 & n_y^2 & 0 \\ 0 & 0 & n_z^2 \end{pmatrix} \quad (4)$$

$$0 = \begin{pmatrix} n_x^2 - n^2(s_y^2 + s_z^2) & n^2 s_x s_y & n^2 s_x s_z \\ n^2 s_x s_y & n_y^2 - n^2(s_x^2 + s_z^2) & n^2 s_y s_z \\ n^2 s_x s_z & n^2 s_y s_z & n_z^2 - n^2(s_x^2 + s_y^2) \end{pmatrix} \begin{pmatrix} E_x \\ E_y \\ E_z \end{pmatrix} \quad (5)$$

Setting the determinant of this matrix to zero gives the effective refractive indices of the polarization eigenstates in a biaxial birefringent medium. Since it returns a quadratic equation of n^2 it has two solutions which are the effective refractive indices N_1 , N_2 for the ordinary and extraordinary ray for the given propagation direction.

$$\begin{aligned}(n_x^2 - n^2)(n_y^2 - n^2)(n_z^2 - n^2) + \\ n^2 [s_x^2 (n_y^2 - n^2)(n_z^2 - n^2) + s_y^2 (n_x^2 - n^2)(n_z^2 - n^2) + s_z^2 (n_x^2 - n^2)(n_y^2 - n^2)] = 0\end{aligned}\quad (6)$$

This derivation was taken from [10] and equation 6 was implemented into NuRadioMC. As an input it takes the direction \vec{s} , the refractive index n and the entries from the dielectric tensor from equation 4. To find the roots of the returned function a minimizer was used to find the minimum and set the limit for the root finder. The roots were then the solutions N_1 and N_2 . This process can be seen in figure 4 where equation 6 is plotted against various values of n . For this plot a toy model was used with $\vec{s} = [1, 1, 1]/\sqrt{3}$, $n_x = 1.777$ and $n_y, n_z = 1.781$.

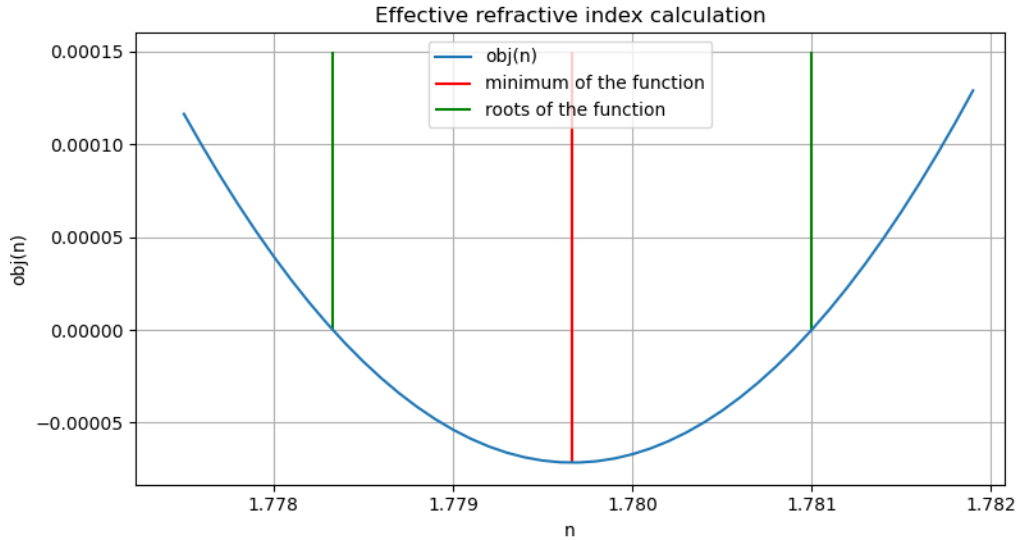


Figure 4: Visualization of the numerical method to find the effective refractive indices via equation 6.

2.2 Time Delay and Polarization

In order to calculate the velocity of the wave traversing a medium at the given direction \vec{s} , the speed of light in vacuum c is divided by the effective refractive index N_i . Including the length of the medium l returns the propagation time t . By subtracting the time calculated from N_1 with the time calculated from N_2 gives the time delay ΔT due to birefringence.

$$\Delta T = \frac{l}{c}(N_1 - N_2) \quad (7)$$

The polarization of the two eigenstates was investigated as well. For $n \neq N_i$ equation

6 can be used to find the direction of the electric field:

$$\vec{E}_i = \begin{pmatrix} \frac{s_x}{N_i^2 - n_x^2} \\ \frac{s_y}{N_i^2 - n_y^2} \\ \frac{s_z}{N_i^2 - n_z^2} \end{pmatrix} \quad (8)$$

In order to take care of the cases where $n_{x,y,z} \approx N_{1,2}$ a few special scenarios were considered. If the wave propagates exclusively into one of the three directions e.g. the x-direction and the effective index of refraction equals approximately the index-of-refraction of one of the other two directions e.g. the y-direction, the polarization points exclusively into the direction in which the values of the indices are similar e.g. $\vec{E} = (0, 1, 0)$. Another special case considers the direction vector being perpendicular to just one of the principal axes e.g. the x-axis. If the effective refractive index is approximately equal to the refractive index of this axis the polarization points into this axis as well e.g. $\vec{E} = (1, 0, 0)$. The precision at which the effective refractive index is approximately equal to one of the directional indices of refraction can be adjusted in the simulations. The polarization vector calculated with equation 8 was then normalized and converted to spherical coordinates.

3 Modeling the refractive index of the Antarctic ice

The 'regular' birefringence occurs in every medium that has different indices of refraction in different directions. However, the ice medium in Antarctica is even more complex. Due to the pressure of the ice and the way that ice accumulates the density of the ice is depending on the depth. Since the index-of-refraction depends on the density of the ice, the three indices-of-refraction for the x, y and z direction also depend on the depth at which they are measured. As can be seen in figure 5 the index-of-refraction changes from about 1.3 at the surface to about 1.78 at a depth of a few km. This density effect is much larger than the differences occurring due to the directional dependence of the permittivity.

3.1 Southpole 2015 Model

The model for the index-of-refraction used in NuRadioMC so far has not taken the directional dependence on the permittivity into account. This model uses equation 9 to calculate the index-of-refraction n depending on the depth z :

$$n(z) = n_{ice} - \Delta n \cdot \exp\left(\frac{z}{z_0}\right) \quad (9)$$

Here $n_{ice} = 1.78$, $\Delta n = 0.423$ and $z_0 = 77$ m. The model was taken from [11]. As can be seen in figure 5 the index-of-refraction stays almost constant up until ~ 500 m where the pressure due to gravity changes the density of the ice.

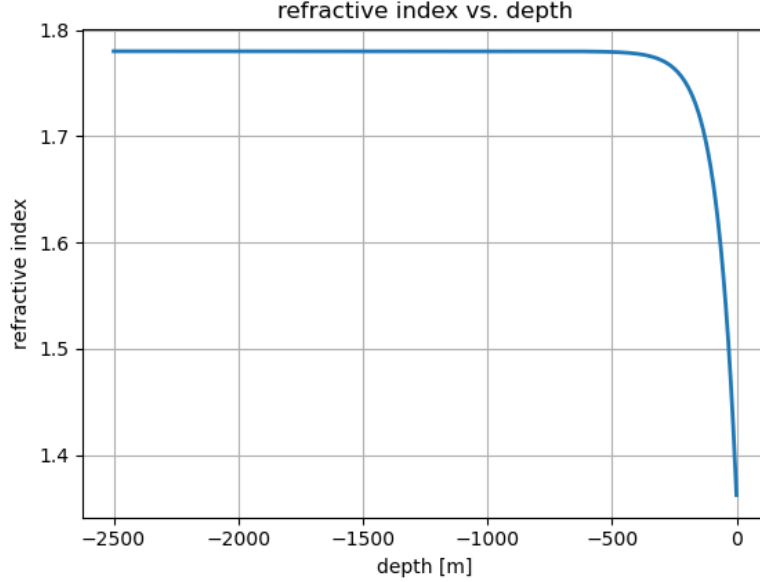


Figure 5: Refractive index as a function of depth. Visualization of equation 9.

3.2 SPICE Data

Since the ice of Antarctica is a biaxial medium it has different permittivities for every direction. The coordinate system is chosen such that the z-axis corresponds to the c-axis of the ice (depth) and that the x-axis points in the direction of the ice flow. For the most part the three components behave similar to the refractive index calculated with 9. However, at higher accuracy one can measure a difference between the three directions. This difference of the eigenvalues representing the relative c-axis concentration E_1 , E_2 , E_3 was measured in the SPICE ice core [12] and used in the birefringence model of [13]. The diagonal matrix elements of equation (Eq. 10) were calculated using $\epsilon'_\perp = 3.157$ and $\Delta\epsilon' = 0.034$ taken from [13].

$$\epsilon_r(z) = \begin{pmatrix} \epsilon_x & 0 & 0 \\ 0 & \epsilon_y & 0 \\ 0 & 0 & \epsilon_z \end{pmatrix} = \begin{pmatrix} \epsilon'_\perp + \Delta\epsilon' E_1 & 0 & 0 \\ 0 & \epsilon'_\perp + \Delta\epsilon' E_2 & 0 \\ 0 & 0 & \epsilon'_\perp + \Delta\epsilon' E_3 \end{pmatrix} = \begin{pmatrix} n_x^2 & 0 & 0 \\ 0 & n_y^2 & 0 \\ 0 & 0 & n_z^2 \end{pmatrix} \quad (10)$$

It has to be noted, that it is not trivial that the matrix for the indices of refraction resulting from the relative permittivities is diagonal. There are biaxial crystal struc-

tures with off diagonal entries in the permittivity matrix. However, for this model the permittivity matrix was assumed to be diagonal.

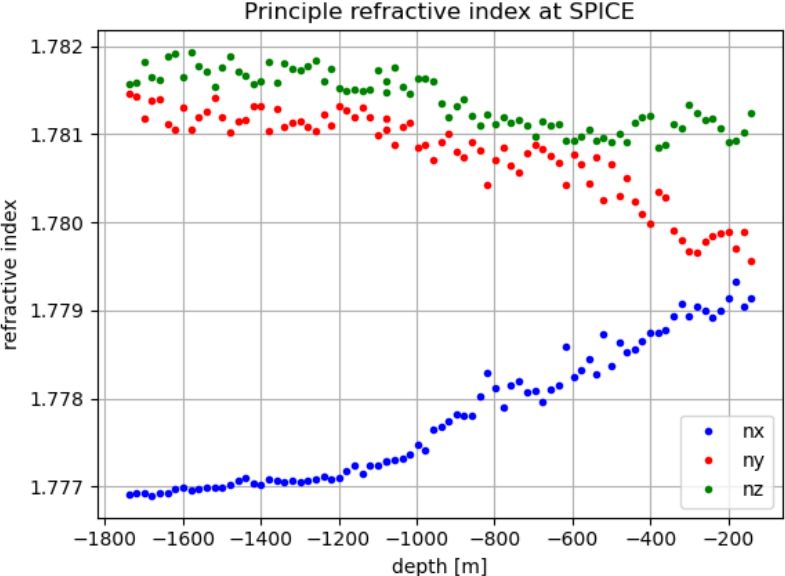


Figure 6: Data set for the refractive indices in x-, y- and z-direction relative to 1.78. Data taken from [12]

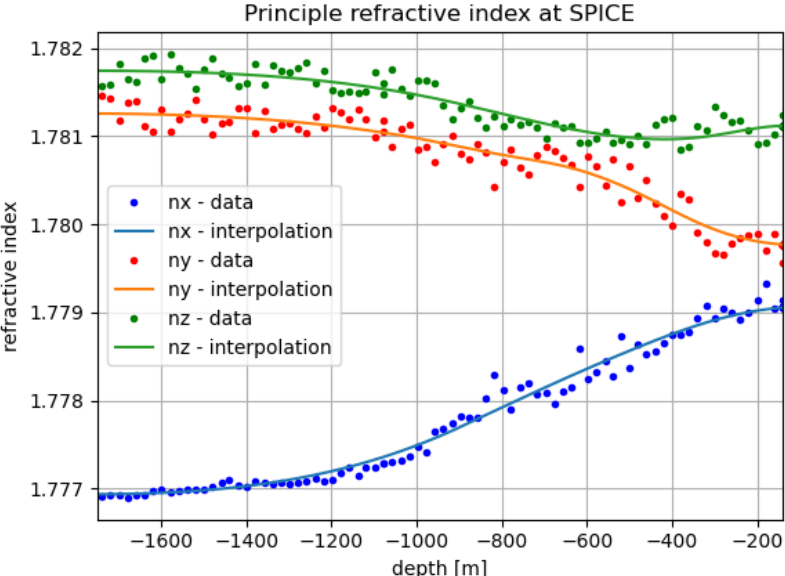


Figure 7: Interpolated data set from figure 6.

With the measurement done by SPICE [12] this calculation results in the data seen in figure 6. It has to be stated that this data set does not include the change of the refractive index due to the depth dependent density change seen in 3.1. It only shows the relative index-of-refraction of the directions compared to a set value of 1.78. Also, this measurement only included the depths from -140 m to -1739 m. In order to properly model the birefringence the refractive index had to range from the surface down to -2500 m. Due to this reason the average refractive index was calculated for the first and the last ten points of each data set and constant values were added at this average for the missing depth values. This ensured that the values for n_x , n_y and n_z to be constant outside of the measured data. This is also an approximation since the values might change at those depths. A spline interpolation was used to approximate the resulting data set. The result can be seen in figure 7.

3.3 Merging of the two Models

In order for the birefringence model to include both effects laid out in the previous chapters figure 5 and figure 7 were combined. To do this the difference between 1.78 and the interpolated values from figure 7 were added to the previously used model that included the density dependency.

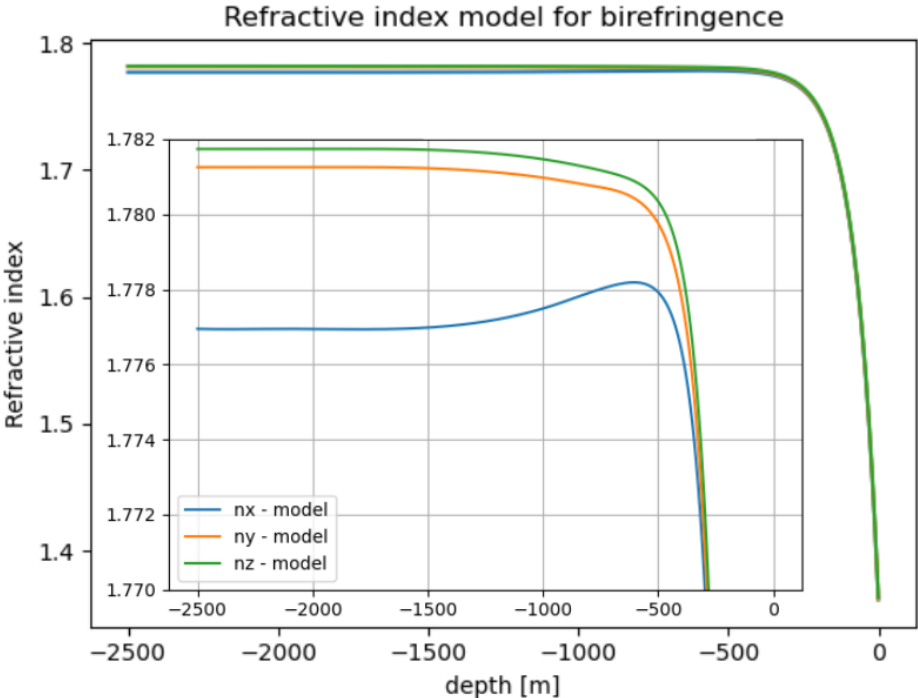


Figure 8: Refractive index as a function of depth. Combination of figure 5 and figure 7. The inner plot is the zoomed in version of the outer plot.

4 Pulse Propagation

The modeling of a pulse propagating through the ice can be subdivided into two parts. The first part focuses on the path the wave takes from the source to the antenna and the second part is how the amplitude of the propagating pulse changes due to changes in the wave propagation direction and its polarization.

4.1 Analytical Ray Tracer

When modeling the path of the wave the main difficulty is the depth dependence on the index-of-refraction. This results in a bending of the radio wave along its trajectory. Due to this bending there are three mayor types of solutions for the path. It can be an almost direct path from the source to the antenna with minimal refraction, it can be a path that would have missed the antenna but due to the major refraction in the firn gets bend downwards again towards the antenna and it can be a path that is reflected at the ice surface and is then detected by the antenna. In a numerical ray tracing model this is calculated in a way that every layer at which the index-of-refraction changes Snell's law has to be satisfied.

$$n_1 \sin(\theta_1) = n_2 \sin(\theta_2) \quad (11)$$

This means those simulations rely on time intensive trial and error calculations to find the path from the source to the antenna. However, when modeling the index of reflection with equation 9, one can also find analytical solutions for the path of the wave.

$$y(z) = \pm z_0 \sqrt{n_{ice}^2 C_0^2 - 1} \cdot \ln \left(\frac{\gamma}{2\sqrt{c(\gamma^2 - b\gamma + c)} - b\gamma + 2c} \right) + C_1 \quad (12)$$

Here, C_0 and C_1 are the initial conditions determined from the source and antenna positions, $\gamma = \Delta n \cdot \exp(z/z_0)$, $b = 2n_{ice}$ and $c = n_{ice}^2 - C_0^{-2}$. From this wave path the time it takes from the source to the antenna can also be estimated.

$$t = \int_{z_1}^{z_2'} \frac{n(z)}{z} \sqrt{1 + \left(\frac{dy(z)}{dz} \right)^2} dz \quad (13)$$

Here, z_1 and z_2' refer to the depth of the path position and can be determined from the initial positions of the source and the antenna. Both of these functions are already implemented into NuRadioMC and for a more detailed description see [6]. The direct, refracted and reflected solutions from the analytical ray tracer can be seen in figure 9.

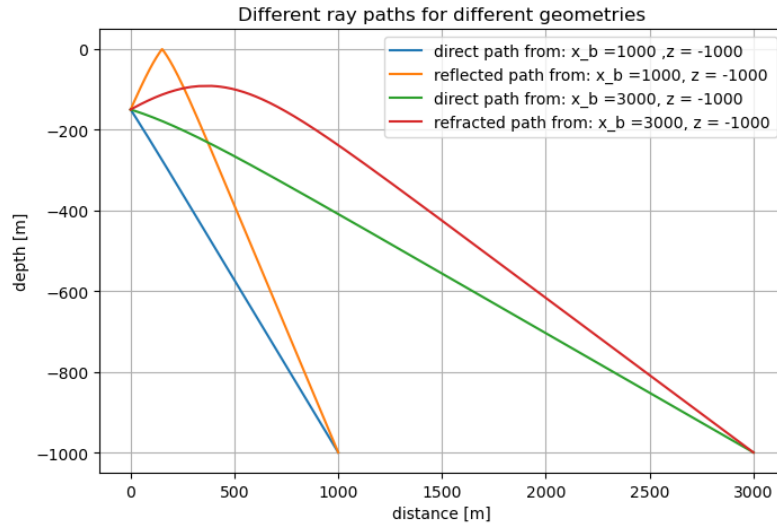


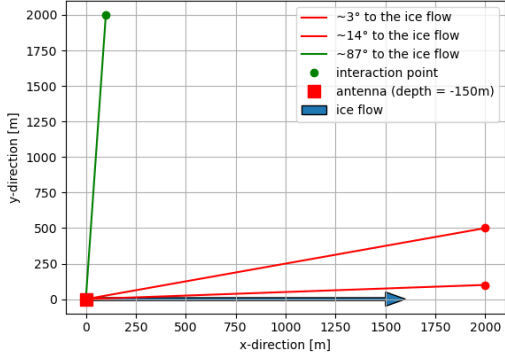
Figure 9: Ray paths calculated with the analytical ray tracer for 2 different geometries. Two direct paths, one refracted and one reflected path can be seen.

As explained in section 1.3, birefringence has the effect of splitting the wave at a refractive surface according to its propagation direction and polarization. As such there are potentially infinitely many different rays between the source and the antenna. The largest birefringence effect in the propagation however, corresponds to the first time this splitting occurs. This means for every solution of the ray tracer there is one 'slow' and one 'fast' component that take slightly different paths. For the calculations in this report the spacial splitting between the 'slow' and the 'fast' component was considered negligible and only the time delay due to different indices-of-refraction was considered as well as the mixing of the two polarization states due to a changing polarization. In this way the 3D version of the analytical ray tracer could still be used and the time delay and the polarization could be calculated for every step of the path via equation 7 and 8. In order to get the total time delay from the source to the antenna all the small time delays for every step of the ray tracer were then added together.

4.2 Pulse Propagation due to Changing Polarization

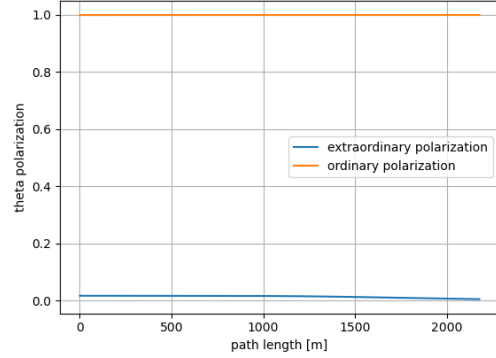
After implementing the proposed birefringence model into the analytical ray tracer of the NuRadioMC code, the polarization along the ray path was investigated. Due to the change of the index-of-refraction and the direction, the polarization was expected to change as well. In spherical coordinates the radial component of the electromagnetic wave was almost zero and the polarization could be represented by the theta and phi component alone.

Azimuthal orientation from: [100 2000 -1000] compared to the ice flow



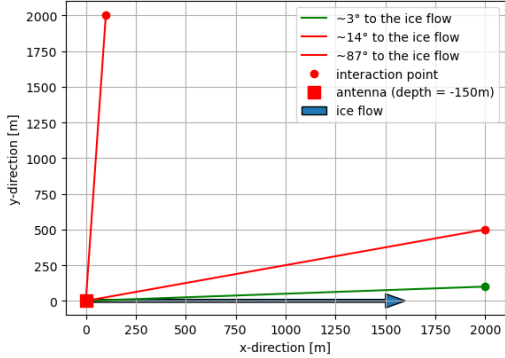
(a)

source position = [100 2000 -1000], receiver position = [0 0 -150]



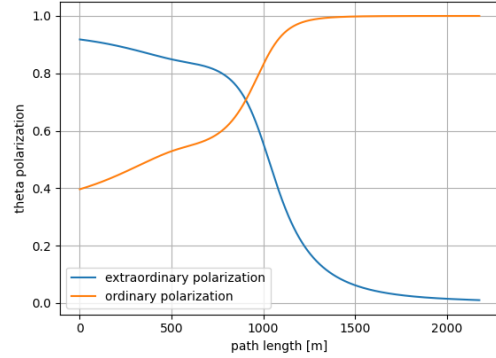
(b)

Azimuthal orientation from: [2000 100 -1000] compared to the ice flow



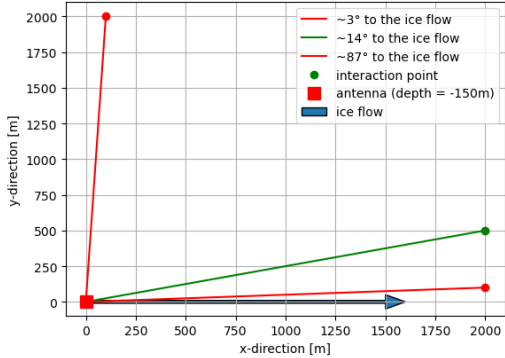
(c)

source position = [2000 100 -1000], receiver position = [0 0 -150]



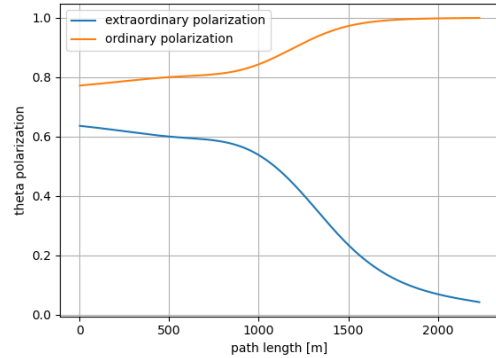
(d)

Azimuthal orientation from: [2000 500 -1000] compared to the ice flow



(e)

source position = [2000 500 -1000], receiver position = [0 0 -150]



(f)

Figure 10: Left: Geometry of the source and antenna position projected on the xy-plane. The starting position and propagation path are indicated in green. The ice flow direction is indicated as a blue arrow. Right: Theta component of the polarization in polar coordinates for the ordinary and extraordinary ray along the ray path. Only the direct rays were considered.

The results from some toy geometries can be seen in figure 10. For these plots the position of the antenna was set to $x = 0$ m, $y = 0$ m and $z = -150$ m. The position of the source is indicated for every plot with a depth of $z = -1000$ m. The geometries were chosen in a way that an azimuthal dependence between the ray path and the ice flow becomes clear. The polarization plots show the absolute, normalized theta component of the polarization vector against the length of the propagation path. For the first geometry seen in figure 10a the polarization seen in figure 10b stays approximately constant. However, for the second geometry seen in figure 10c the polarization seen in figure 10d changes drastically about half way through the ray path. The polarization of the ordinary and extraordinary ray seem to flip through the course of the path. For the third geometry seen in figure 10e the polarization seen in figure 10f also changes about half way through the ray path, but not as much as in the second case. These results show a clear dependence between the polarization change and the azimuthal direction of the ray. The biggest change of polarization is most likely caused, as the ray enters the top ~ 500 m of the ice sheet where the density change of the ice becomes a major contribution to the refractive index. For completeness the polarization of the refracted and reflected ray was visualized as well and can be seen in figure 11. As the polarization vector is calculated via the electric field, the sign change in the z-component of the direction vector results in a sharp polarization change for both of these special cases.

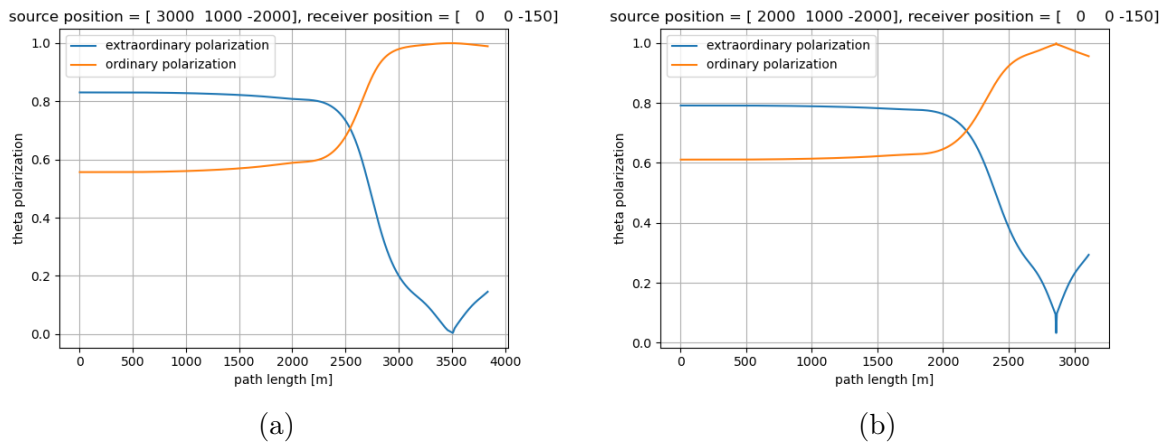


Figure 11: Polarization change for a refracted ray from $x = 3000$ m, $y = 1000$ m and $z = -2000$ m (11a). Polarization change for a reflected ray from $x = 2000$ m, $y = 1000$ m and $z = -2000$ m (11b).

With the results from figure 10, the question of modeling birefringence becomes more complicated. As the polarization changes both the ordinary and extraordinary ray get split further as they now have a fast and slow component themselves. Therefore, for every step of the simulation the number of rays doubles if there is a change in the

polarization. This also means that the signal measured at the antenna could be smeared out as the polarization changes. This could potentially lead to smaller signal amplitudes and possibly even missing the trigger level to measure one of the signals. To quantify how big this effect would be the pulse propagation in the ice was modeled. Two time traces were created with a length proportional to the time delay. One for the ordinary and one for the extraordinary ray. This was done by applying a Fourier transformation to a delta pulse and then cutting out frequencies over 500 MHz. For every step of the ray tracer those time traces were then adjusted to represent the signal pulses at this point. To do this a rotation matrix (Eq. 14) with the polarization entries was used to transfer the polarization states into the time domain of the 'fast' and 'slow' ray (Eq. 15). Then, the small time shift for the corresponding lengths was applied to the 'fast' trace (Eq. 16). Then the inverse of the rotation matrix was used to rotate back into the polarization states theta and phi (Eq. 17). As the polarization changes, the rotation matrix changes for every infinitesimal step and the pulses propagate while mixing according to this change.

$$R = \begin{pmatrix} \Theta & -\Phi \\ \Phi & \Theta \end{pmatrix} \quad (14)$$

$$\begin{pmatrix} t_{slow} \\ t_{fast} \end{pmatrix} = R \begin{pmatrix} t_{\Theta} \\ t_{\Phi} \end{pmatrix} \quad (15)$$

$$t_{fast} \rightarrow t_{fast} + \Delta t \quad (16)$$

$$\begin{pmatrix} t_{\Theta} \\ t_{\Phi} \end{pmatrix} = R^{-1} \begin{pmatrix} t_{slow} \\ t_{fast} \end{pmatrix} \quad (17)$$

This process of rotating and shifting the time difference can be seen in figure 12. In step 0 the two pulses are created and overlap each other since there was no propagation yet. Step one represents the rotation of the polarization states into the time domain (Eq. 15) with arbitrary values of $\theta = 0.8$ and $\phi = 0.6$. Step two represents the time shift performed by equation 16 with the arbitrary value of $\Delta t = 10\text{ns}$. Step three then shows the rotation back to the polarization states theta and phi using equation 17. The steps 1-3 are then repeated for every step of the ray tracer and the time delay which should be measured at the antenna can be simulated while mixing the polarization states along the way.

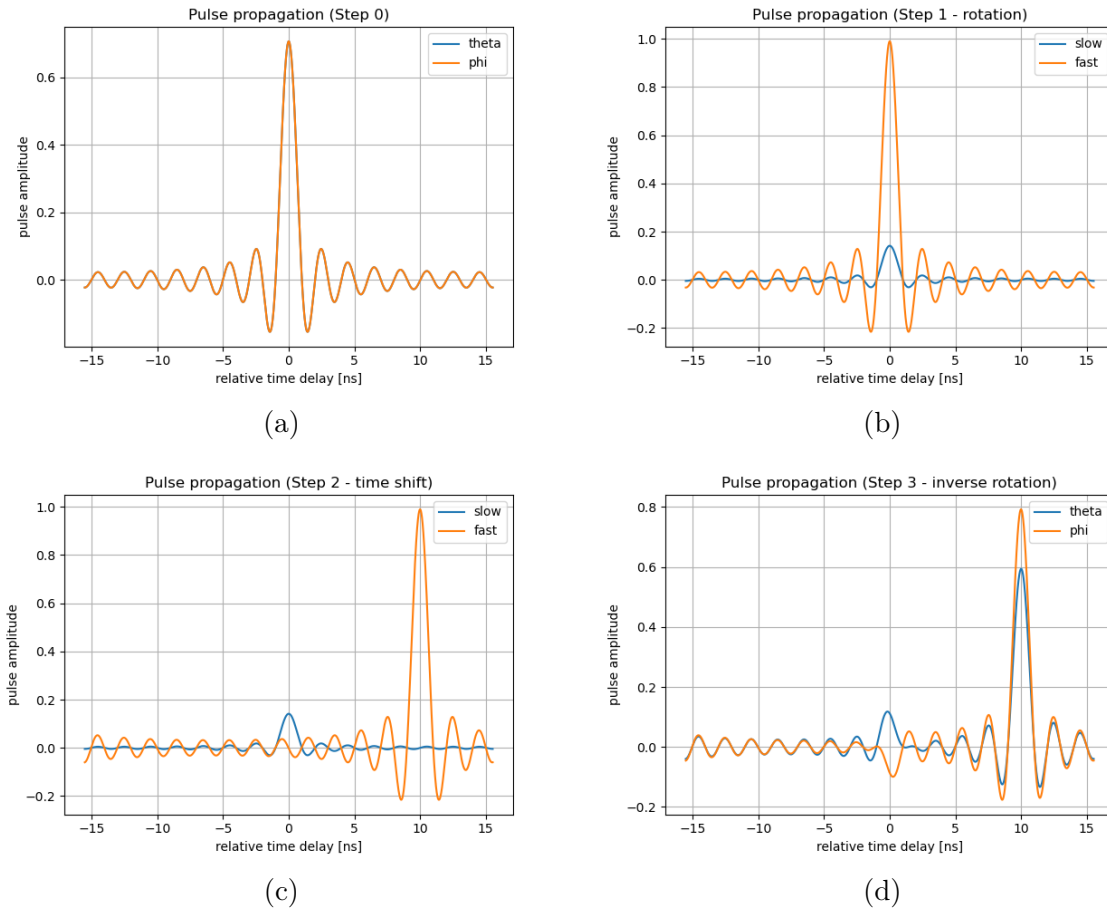


Figure 12: Pulse propagation model with the created time traces at the source (12a), the rotation into the time domain (12b), the time shift applied to the faster pulse (12c) and the inverse rotation back into the polarization states (12d).

5 Results for different Geometries

So far, there have already been attempts to simulate and measure the birefringence induced time delay. The results from the time delay calculation, the polarization calculation and the pulse propagation of the introduced model will be compared to the existing simulations and data from the ARA experiment presented in [13]. For this comparison only the direct ray of the model will be used. However, the refracted ray showed interesting properties as well. Namely, that the birefringence induced time delay appears to be smaller in the refracted ray compared to the direct ray even though the propagation length is longer. This can be traced back to the steeper inclination angle of the refracted ray compared to the direct ray.

5.1 Comparing the model to ARA measurements

The ARA experiment, located at the South Pole, has started to investigate birefringence effects on radio wave propagation. The receiver stations A2 and A4 are composed of different antenna geometries at slightly various depths and positions. The depth of the antennas was approximated with -150 m. The approximate baselines and angles to the ice flow from the sources to the antennas can be seen in table 1. It has to be noted that the used and displayed geometries are only approximations to the real geometries and the main focus was whether the acquired values for the time delay behave similar as in [13].

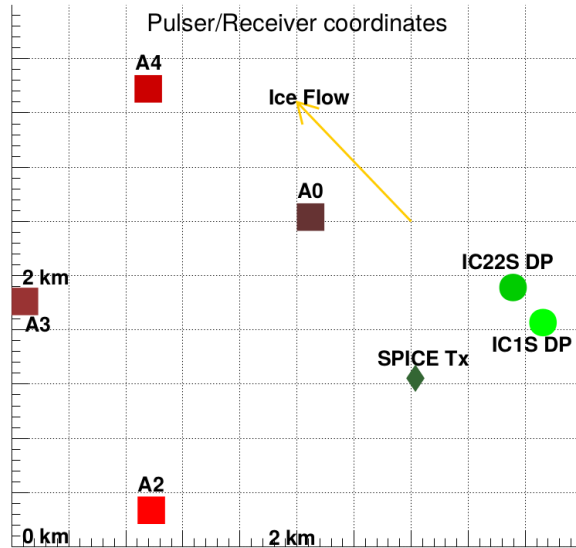
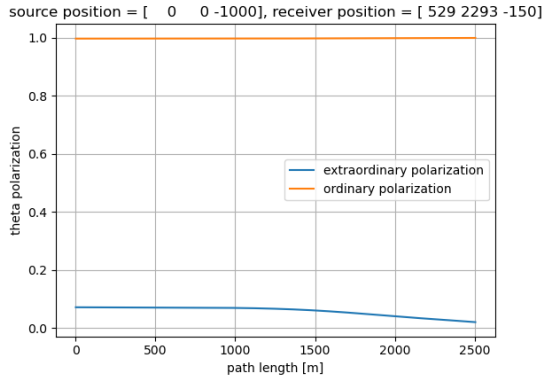


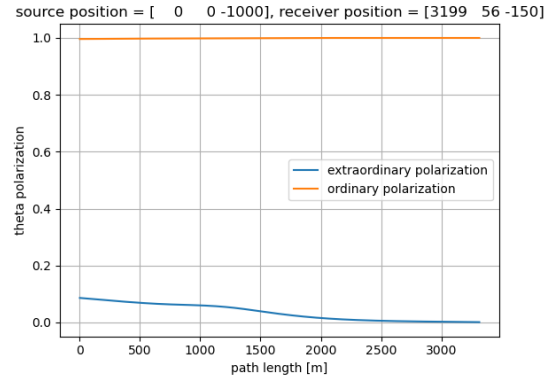
Figure 13: The geometry of the relevant ARA stations with SPICE and the deep pulser (DP) sources and the antennas A2 and A4. The direction of the ice flow is indicated as yellow. Taken from [13].

source - antenna	baseline [m]	angle to ice flow
SPICE - A2	2353	77°
SPICE - A4	3702	1°
DP - A2	3199	79°
DP - A4	3700	18°

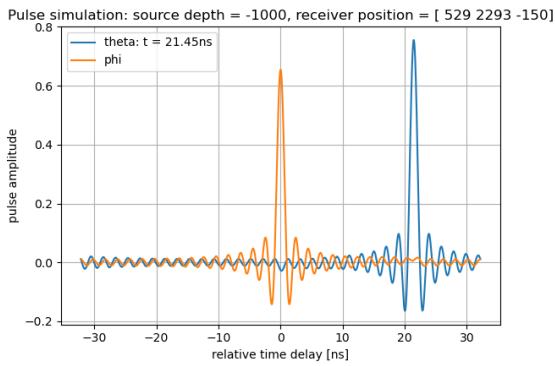
Table 1: Baseline and angle to ice flow values used for the different geometries. Taken from [13].



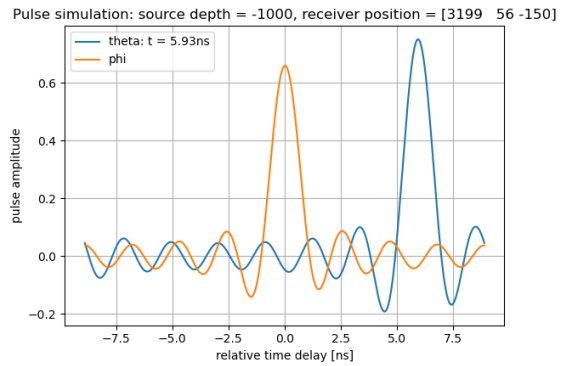
(a)



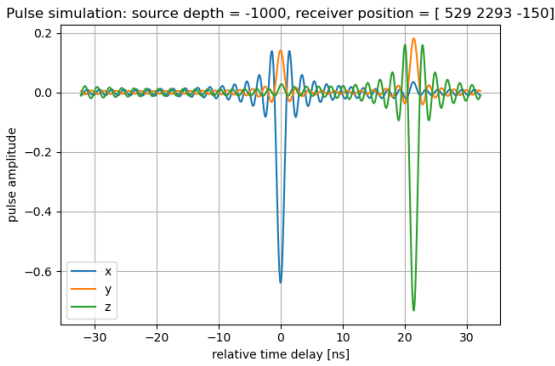
(b)



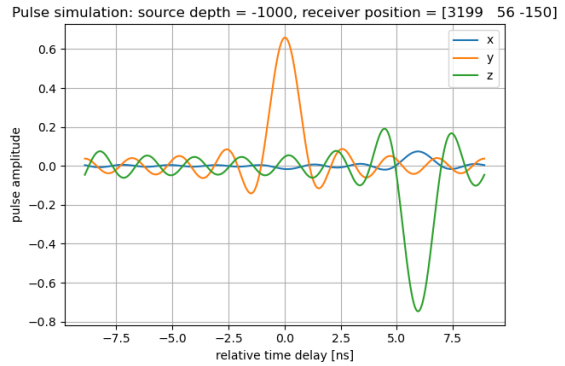
(c)



(d)

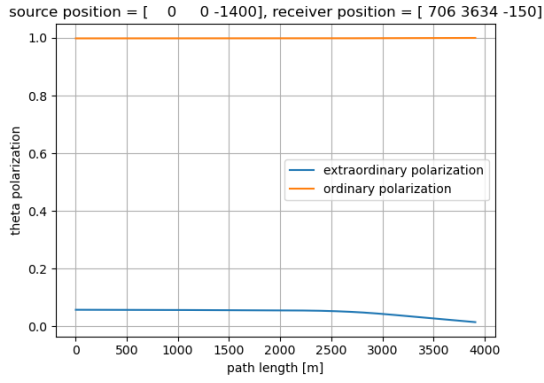


(e)

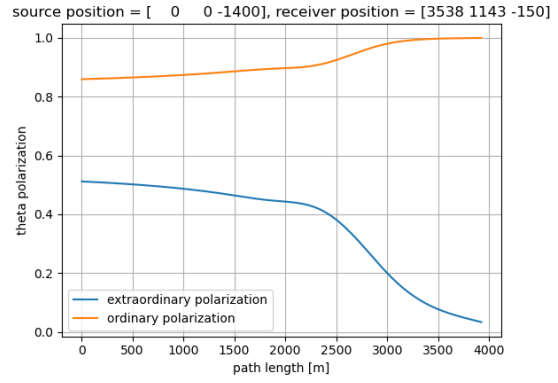


(f)

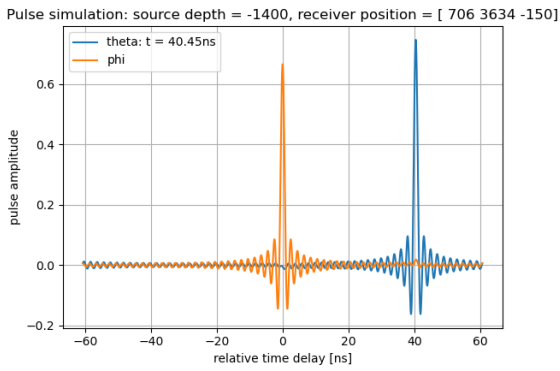
Figure 14: Simulation of the polarization (top), pulse propagation in polar (center) and Cartesian (bottom) coordinates from the SPICE core source to the A2 receiver (left) and the SPICE core source to the A4 receiver (right).



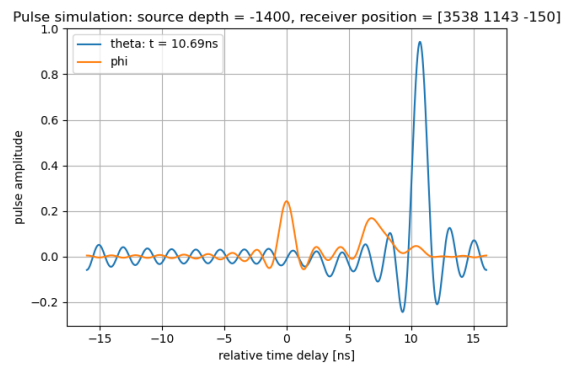
(a)



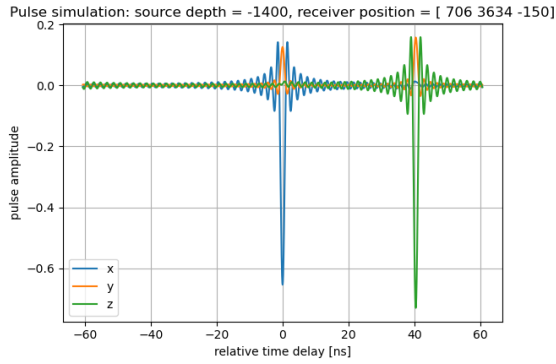
(b)



(c)



(d)



(e)



(f)

Figure 15: Simulation of the polarization (top), pulse propagation in polar (center) and Cartesian (bottom) coordinates from the deep pulser source to the A2 receiver (left) and the deep pulser source to the A4 receiver (right).

The first geometry that was investigated was the SPICE source to the A2 antenna. As seen in figure 13 the propagation path is almost perpendicular to the ice flow. Judging from figure 10b the polarization along the path was not expected to undergo major changes for this type of geometry. This was confirmed by figure 14a. The time delay for this geometry was calculated to be $\Delta T = -21.45$ ns. Due to the small changes in the polarization not a lot of mixing in the pulse propagation was to be expected either. As seen in figure 14c this was confirmed by the simulation. Only a small change in amplitude between the two pulses is visible. By using the propagation direction at the antenna position the polar representation of the time traces was converted back into Cartesian coordinates. This can be seen in figure 14e. Here, it can be seen that the slower pulse is a mixture of the polarization in x- and y-direction while the faster pulse is a mixture between the polarization in z- and y-direction.

For the second geometry with SPICE as the source and A4 as the antenna more changes in the polarization were expected judging from figure 10d for this type of geometry. However, as can be seen in figure 14b this was not the case. It seems that other than the earlier explained azimuthal dependence on the polarization there is a zenithal dependence on the polarization as well since the horizontal distance from the source is larger while the depth of the source stayed the same. This zenithal dependence on the polarization change is not in the scope of this report but it should be investigated further in the future. The time delay for this geometry was calculated to be $\Delta T = -5.93$ ns. For the pulse propagation this meant that there was not much mixing to be expected either since the polarization did not show the expected change. This can be seen in figure 14f where again only a small change in the amplitudes is visible. For the propagated pulses in Cartesian it is interesting to see that now the slower pulse is dominated by the polarization in y-direction while the faster pulse is dominated by the polarization in z-direction. The polarization in x-direction only has a small effect on the faster pulse.

The third geometry used the deep pulser as a source and A2 as the antenna. Once again there was not much polarization change expected due to the perpendicular direction to the ice flow. This was confirmed by the data seen in figure 15a. The time delay for this geometry was calculated to be $\Delta T = -40.45$ ns. For the pulse propagation the situation was very similar to the SPICE - A2 geometry with minimal change in the pulse amplitude even though the calculated time delay was almost twice as large. Also the pulses in Cartesian coordinates are very similar to the SPICE - A2 geometry with the polarization in x-direction contributing mostly to the slow pulse, the polarization in z-direction contributing mostly to the fast pulse and the y-direction making minor contributions to both pulses.

The fourth geometry using the deep pulser source and the A4 antenna was perhaps the most interesting considering the model that was used. It showed a relatively big change in the polarization along the path (figure 15b). This was consistent with the polarization calculated with the third toy geometry in 10f. This also resulted in a mixing between the two polarization states along the path as can be seen in figure 15d

and 15f. The amplitude of the slower pulse is much smaller than the fast pulse. Also, the fast pulse has a second, smaller peak due to the mixing of the polarization states. The polarization of the y-direction is contributing to the slow peak and the second peak of the fast pulse while the polarization of the z-direction is mainly contributing to the fast pulse. The polarization of the x-direction is contributing to all three peaks but with a very small amplitude in each of them.

source - antenna	receiver position x,y,z (m)	source position x,y,z (m)	ΔT_{calc} (ns)	ΔT_{sim} (ns)	ΔT_{exp} (ns)
SPICE - A2	[529, 2293, -150]	[0, 0, -1000]	-21.45	-22.5	-14.1 ± 2.8
SPICE - A4	[3199, 56, -150]	[0, 0, -1000]	-5.93	-1.6	4.6 ± 9
DP - A2	[706, 3634, -150]	[0, 0, -1400]	-40.45	-42.5	-25.2 ± 2.0
DP - A4	[3538, 1143, -150]	[0, 0, -1400]	-10.69	-0.2	0.7 ± 1.4

Table 2: Time delay comparison to [13]. ΔT_{calc} is the time delay calculated by the model presented in this report, ΔT_{sim} and ΔT_{exp} are the time delays simulated and measured in [13].

5.2 Numerical accuracy

As a first accuracy check the times from source to antenna from the ordinary and extraordinary ray were compared to the travel time calculated from equation 13. For all four presented geometries the travel time calculated by equation 13 (in the range of micro seconds) was between the calculated travel times for the ordinary and extraordinary ray.

As a second accuracy check the step number of the ray tracer was increased to get more accurate results for the time delay calculation and the pulse propagation. So far, all results presented used the same number of steps in the ray tracer: 1000. In order to investigate the numerical accuracy of the model, the time delay, polarization and the pulse propagation was simulated for one geometry with different orders of magnitude of accuracy. The geometry used was the deep pulser source and the A4 antenna since this showed the most interesting mixing properties. The results for the time delay can be seen in table 3 and figure 16. Here, the time delay was calculated for $10^2 - 10^6$ steps in the analytical ray tracer. As a conservative estimate for the numerical error at 1000 steps ± 0.01 ns was used. Obviously, the accuracy does not only depend on the amount of steps taken by the ray tracer but also the geometry used. If one investigates sources > 10 km away from the antenna the step number would have to be increased in order to maintain the accuracy. Since the attenuation of radio waves in ice restricts the distance at which one can measure the signal it is unlikely that one would want to investigate such geometries.

number of steps in the ray tracer	step size [m]	calculated time delay [ns]
10	~ 467	-10.43853
100	~ 48	-10.66927
1000	~ 4.9	-10.68909
10000	~ 0.49	-10.69104
100000	~ 0.049	-10.69124
1000000	~ 0.0049	-10.69126

Table 3: Time delay comparison for different numerical accuracies.

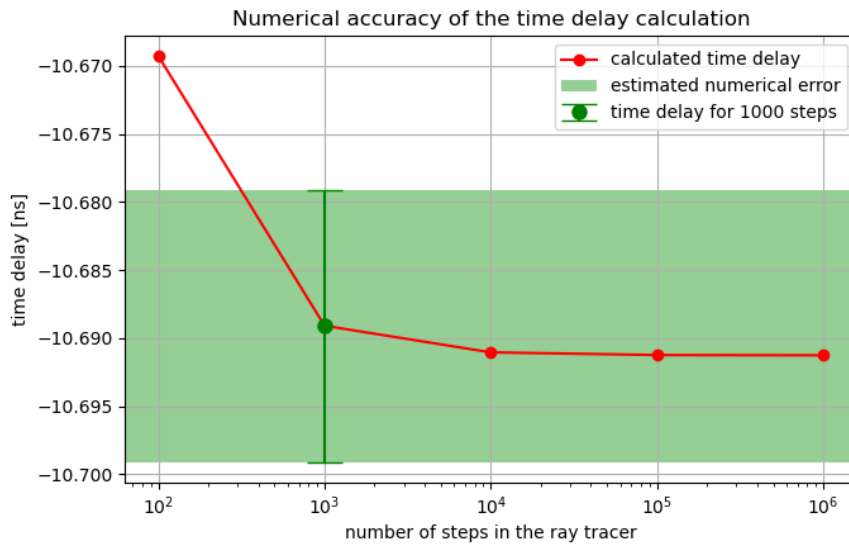


Figure 16: Time delay comparison for different numerical accuracies. The calculated time delay approaches a more accurate value with the increase in the step number. The green area covers the ± 0.01 ns error around the time delay for which 1000 steps were used.

Figure 17 shows the pulse propagation using 1000 steps overlapping the pulse propagation using 100000 steps. There is no visible difference between the two simulations for the the same geometry. From the time delay and pulse propagation comparison it is concluded, that 1000 steps in the ray tracer is sufficient for the most relevant geometries.

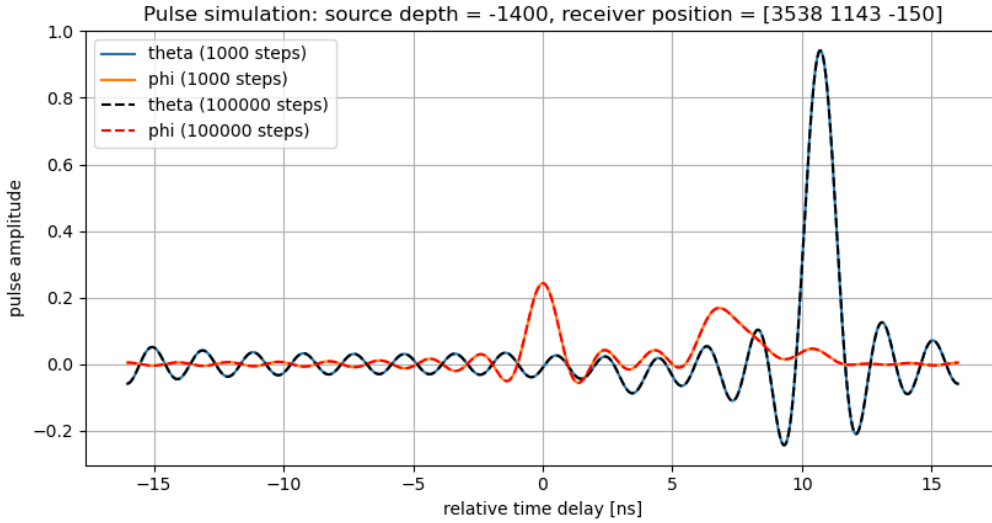


Figure 17: Pulse propagation for a simulation using 1000 steps in the solid blue and orange lines compared to a pulse propagation for a simulation using 100000 steps in the dashed black and red lines.

6 Summary and Outlook

For this report birefringence effects were simulated for the purpose of high-energy neutrino detection. The model used was derived from the Maxwell equations assuming a diagonal biaxial dielectric tensor. From this model the relative time delay between the two resulting polarization states could be calculated as well as their polarization. In order to use the model the refractive indices and the propagation direction vector had to be known at every depth. To model the refractive indices the currently used model with an exponential density dependence was combined with dielectric measurements with directional dependence from [13]. The direction vector was calculated from the analytical ray tracer already implemented in NuRadioMC by neglecting the spacial splitting of the two polarization states.

After investigating the polarization along the propagation path for different geometries an azimuthal dependence became visible. If the propagation direction was similar to the direction of the ice flow there was a major change in the polarization direction of the two polarization states. If the propagation direction was similar to the direction perpendicular to the ice flow there was little to no change in the polarization of the two states. Later simulations also showed a zenithal dependence of the direction on the polarization change but this effect was not further investigated for this report. As the polarization changed for some geometries along the propagation path it was expected to result in a mixing between the two polarization states. This was investigated by simulating pulses with time traces, rotating them into the time domain, shifting the

faster of the two pulses by the calculated amount and rotating back into the polarization states. This process was repeated along the calculated path for every infinitesimal step of the ray tracer. It was shown that the process of mixing polarization states can lead to signals too low for a set trigger level or to smeared out pulse shapes for which the arrive time might not be clearly identifiable.

The described model was then used to approximate the time delay simulations made in [13]. For the SPICE - A2 geometry this model predicted a time delay of -21.45 ns while [13] predicted -22.5 ns. For the SPICE - A4 geometry this model predicted a time delay of -5.93 ns while [13] predicted -1.6 ns. For the deep pulser - A2 geometry this model predicted a time delay of -40.45 ns while [13] predicted -42.5 ns. For the deep pulser - A4 geometry this model predicted a time delay of -10.69 ns while [13] predicted -25.2 ns. Overall, the proposed model shows similar behavior for the presented geometries even though it uses different ray tracing and refractive index models. The pulse propagation showed the most interesting behavior when the polarization changed along the propagation path which was not the case for three out of the four geometries due to the azimuthal and zenithal dependence on the polarization and polarization change. However, it showed that birefringence induced time delays are a viable option in determining the distance between the neutrino vertex and the antenna even though the mixing of the pulses can cause problems when detecting these radio pulses.

Moving forward it would be important to make the code more efficient and faster especially for the time delay calculation and for the pulse propagation. This could be done splitting the path the analytical ray tracer returns more efficiently according to the changes of the refractive indices. In this way the simulation would do smaller steps in the areas where the refractive index changes a lot and bigger steps when they stay almost constant. Also, the pulse propagation could be made faster by creating shorter time traces which focus on only describing the propagating pulse and not the areas where the amplitude is close to 0. If these changes are made this model could be very useful at simulating the propagation of many radio waves induced by neutrino interactions with various energies, interaction points and directions. Also, more data is available from the ARA experiment from other antenna stations than A2 and A4. Other stations located at about $\sim 45^\circ$ with respect to the ice flow and the antenna would be very useful at investigating the different polarization changes and pulse propagation from these geometries. The final goal of birefringence modeling is, other than having a better understanding of the radio propagation in ice, estimating the distance of the initial neutrino interaction given the measured time delay and direction. In principle this could be done in the future using this birefringence model.

References

- [1] M. Ackermann *et al.*, “Astrophysics uniquely enabled by observations of high-energy cosmic neutrinos,” *Bulletin of the American Astronomical Society*, vol. 51, no. 3, p. 185, 2019. arXiv: [1903.04334].
- [2] P. Allison *et al.*, “Design and initial performance of the askaryan radio array prototype EeV neutrino detector at the south pole,” *Astroparticle Physics*, vol. 35, p. 457, 2012. arXiv: [1105.2854].
- [3] A. Anker *et al.*, “Targeting ultra-high energy neutrinos with the ARIANNA experiment,” *Advances in Space Research*, vol. 64, no. 12, p. 2595–2609, 2019. arXiv: [1903.01609].
- [4] J. Aguilar *et al.*, “Design and sensitivity of the radio neutrino observatory in greenland (RNO-G),” *Journal of Instrumentation*, vol. 16, no. 03, p. P03025, 2021. arXiv: [2010.12279].
- [5] S. W. Barwick and C. Glaser, “Neutrino physics and astrophysics, chapter 6: Radio detection of high energy neutrinos in ice.” in preperation.
- [6] C. Glaser *et al.*, “NuRadioMC: Simulating the radio emission of neutrinos from interaction to detector,” *The European Physical Journal C*, vol. 80, no. 2, 2020. arXiv: [1906.01670].
- [7] M. Born and E. Wolf, *Principles of Optics: 60th Anniversary Edition*. Cambridge University Press, 7 ed., 2019.
- [8] S. Hindi, “Birefringence of bio-based liquid crystals,” *BioCrystals Journal*, vol. 1, pp. 13–25, 2016. doi: https://www.researchgate.net/publication/299200951_Birefringence_of_bio-based_liquid_crystals.
- [9] Centre for Ice and Climate, “Ice crystal structure,” doi: https://www.iceandclimate.nbi.ku.dk/research/flowofice/ice_crystal_structure/.
- [10] P. Kužel, “Electromagnetism of continuous media,” 2001. doi: <https://www.fzu.cz/~kuzelp/Optics/Lectures.htm>.
- [11] S. Barwick *et al.*, “Observation of classically `forbidden' electromagnetic wave propagation and implications for neutrino detection.,” *Journal of Cosmology and Astroparticle Physics*, vol. 2018, no. 07, pp. 055–055, 2018. arXiv: [1804.10430].
- [12] D. E. Voigt, “c-axis fabric of the south pole ice core, spc14,” *U.S. Antarctic Program (USAP) Data Center*, 2017. doi: <https://doi.org/10.15784/601057>.

- [13] T. M. Jordan *et al.*, “Modeling ice birefringence and oblique radio wave propagation for neutrino detection at the south pole,” *Annals of Glaciology*, vol. 61, no. 81, p. 84–91, 2020. arXiv: [1910.01471].
- [14] S. Fujita *et al.*, “Radio-wave depolarization and scattering within ice sheets: a matrix-based model to link radar and ice-core measurements and its application,” *Journal of Glaciology*, vol. 52, no. 178, p. 407–424, 2006. doi: <https://doi.org/10.3189/172756506781828548>.
- [15] K. Matsuoka *et al.*, “Effects of birefringence within ice sheets on obliquely propagating radio waves,” *IEEE Transactions on Geoscience and Remote Sensing*, vol. 47, no. 5, pp. 1429–1443, 2009. doi: 10.1109/TGRS.2008.2005201.
- [16] I. Kravchenko *et al.*, “Radio frequency birefringence in south polar ice and implications for neutrino reconstruction,” *Astroparticle Physics*, vol. 34, no. 10, pp. 755–768, 2011. doi: <https://www.sciencedirect.com/science/article/pii/S0927650511000168>.
- [17] A. Connolly, “Impact of biaxial birefringence in polar ice at radio frequencies on signal polarizations in ultra-high energy neutrino detection,” 2021. arXiv: [2110.09015].
- [18] N. Harty, “Modeling radio wave propagation in anisotropic ice,” 2021.